Direct numerical simulations of spiral Taylor–Couette turbulence

Pieter Berghout[1,†], **Rick J. Dingemans**[1], **Xiaojue Zhu**[1,2],
Roberto Verzicco[1,3,4], **Richard J. A. M. Stevens**[1], **Wim van Saarloos**[5]
and Detlef Lohse[1,6,†]

[1]Physics of Fluids Group and Max Planck Center Twente, MESA+ Institute and J. M. Burgers Centre for Fluid Dynamics, University of Twente, P.O. Box 217, 7500AE Enschede, Netherlands

[2]Center of Mathematical Sciences and Applications, and School of Engineering and Applied Sciences, Harvard University, Cambridge, MA 02138, USA

[3]Dipartimento di Ingegneria Industriale, University of Rome 'Tor Vergata', Via del Politecnico 1, Roma 00133, Italy

[4]Gran Sasso Science Institute - Viale F. Crispi, 7, 67100 L'Aquila, Italy

[5]Instituut-Lorentz, Universiteit Leiden, Postbus 9506, 2300 RA, Leiden, The Netherlands

[6]Max Planck Institute for Dynamics and Self-Organisation, Am Fassberg 17, 37077 Göttingen, Germany

We perform direct numerical simulations of spiral turbulent Taylor–Couette (TC) flow for $400 \leqslant Re_i \leqslant 1200$ and $-2000 \leqslant Re_o \leqslant -1000$, i.e. counter-rotation. The aspect ratio $\Gamma = \text{height/gap width}$ of the domain is $42 \leqslant \Gamma \leqslant 125$, with periodic boundary conditions in the axial direction, and the radius ratio $\eta = r_i/r_o = 0.91$. We show that, with decreasing Re_i or with decreasing Re_o, the formation of a turbulent spiral from an initially 'featureless turbulent' flow can be described by the phenomenology of the Ginzburg–Landau equations, similar as seen in the experimental findings of Prigent *et al.* (*Phys. Rev. Lett.*, vol. 89, 2002, 014501) for TC flow at $\eta = 0.98$ an $\Gamma = 430$ and in numerical simulations of oblique turbulent bands in plane Couette flow by Rolland & Manneville (*Eur. Phys. J.*, vol. 80, 2011, pp. 529–544). We therefore conclude that the Ginzburg–Landau description also holds when curvature effects play a role, and that the finite-wavelength instability is not a consequence of the no-slip boundary conditions at the upper and lower plates in the experiments. The most unstable axial wavelength $\lambda_{z,c}/d \approx 41$ in our simulations differs from findings in Prigent *et al.*, where $\lambda_{z,c}/d \approx 32$, and so we conclude that $\lambda_{z,c}$ depends on the radius ratio η. Furthermore, we find that the turbulent spiral is stationary in the reference frame of the mean velocity in the gap, rather than the mean velocity of the two rotating cylinders.

Key words: Taylor–Couette flow, pattern formation, rotating turbulence

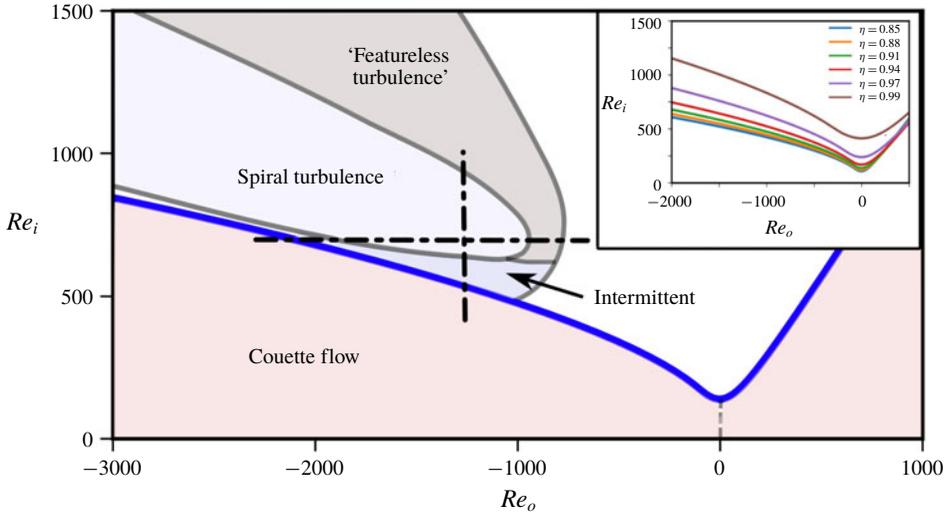† Email addresses for correspondence: p.berghout@utwente.nl, d.lohse@utwente.nl

FIGURE 1. Simplified phase space of low Reynolds TC flow. The blue line is the stability boundary at $\eta = r_i/r_o = 0.91$, as considered in this study, calculated with equation (8) of Esser & Grossmann (1996). The intermittent, spiral turbulence, and 'featureless turbulent' regimes are schematics, indicating the approximate locations of the phases at $\eta = 0.91$, similar to the phase diagram at lower radius ratio ($\eta = 0.84$) in Andereck, Liu & Swinney (1986). The horizontal and vertical dashed-dotted lines represent the simulations that are performed in this paper. The inset shows the stability boundaries for varying η.

1. Introduction

The coexistence of spatially and/or temporally intermittent turbulent and laminar flow regions is one of the most captivating phenomena in fluid mechanics (Barkley & Tuckerman 2005; Barkley 2016). In Taylor–Couette (TC) flow, the flow between two independently rotating concentric cylinders, not too far above the onset of instabilities these patterns manifest themselves as distinctive intertwined bands of laminar and turbulent spirals. Although already observed by Coles (1965) and Van Atta (1966), and famously commented on by Feynman (1964), the origin and dynamics of these patterns remain elusive.

Figure 1 presents a simplified phase space of TC flow with inner cylinder Reynolds numbers $Re_i \leqslant O(10^3)$, (where $Re_i = u_i d/\nu$, with gap width d, inner cylinder velocity u_i and kinematic viscosity ν) and a counter or co-rotating outer cylinder with $-3000 \leqslant Re_o \leqslant 1000$ (where $Re_o = u_o d/\nu$, with outer cylinder velocity u_o). In figure 1, at high inner cylinder Reynolds number Re_i, the flow occupies the 'featureless turbulent' state. With decreasing Re_i, a coherent, spatio-temporal intermittent, turbulent domain appears – spiral turbulence. On further decreasing Re_i, the spiral structure loses coherence and breaks up into intermittent turbulent spots. Below the Taylor stability boundary (Taylor 1923) the flow becomes entirely laminar. The radius ratio dependence of the stability boundary $Re_{i,cr}$ at which the flow undergoes a transition from laminar to intermittently turbulent was derived by Esser & Grossmann (1996) as

$$\left(\frac{Re_i}{Re_{i,lc}} - \frac{Re_o}{\eta Re_{i,lc}}\right)^2 \frac{r_n^2 - r_p^2}{r_p^2} \frac{(1+\eta)^2}{(1-\eta)(3+\eta)} = f\left(a\frac{d_n}{d}\right)^{-4}, \tag{1.1}$$

where the critical Reynolds number for the case of a resting outer cylinder is $Re_{i,lc}(\eta) = (1+\eta)^2/(2\eta\alpha^2((1-\eta)(3+\eta))^{1/2})$ with $\alpha = 0.1556$, and $r_p = r_i + (d/2)f(a(d_n/d))$, the radius of neutral stability $r_n = r_o((Re_i - \eta Re_o)/(Re_i - \eta^{-1}Re_o))^{1/2}$, $d_n = r_n - r_i$, $a(\eta) = (1-\eta)(\sqrt{(1+\eta)^3/(2(1+3\eta))} - \eta)^{-1}$ and the function $f(x) = x$ if $x < 1$ and $f(x) = 1$ if $x \geqslant 1$. Equation (1.1) is shown as the blue line in figure 1. Similar diagrams at different η are found in figure 2(a) of Prigent *et al.* (2002) and figure 1 in Andereck *et al.* (1986).

1.1. *Spiral turbulence*

The first studies on spiral turbulence in TC flow go back to Coles (1965) and Van Atta (1966), who noticed a 'catastrophic' transition to turbulence if the outer cylinder rotates faster than the inner cylinder. In contrast, for pure inner cylinder rotation they observed a transition by 'spectral evolution', meaning that the complexity of the flow gradually increases with increasing inner cylinder Reynolds number. However, the 'catastrophic' transition does not lead to a 'featureless turbulent' flow directly, but rather forms a state of distinct turbulent and laminar domains, which at specific conditions form regular patterns – spirals. The angular velocity of the spiral was found to be very close to $\omega_s = 2(\omega_i + \omega_o)$, where ω_i and ω_o are the inner and outer cylinder angular velocities, respectively. Furthermore, Van Atta (1966) observed strong hysteresis of the spiral turbulence region when approaching the stability boundary from either the 'featureless turbulence' regime or the Couette flow regime. Later, Hegseth *et al.* (1989) observed that the pitch angle of the spiral is non-uniform, and showed that this fits well into a framework of phase dynamics, with the phase being represented by the mean azimuthal position of the spiral. The boundary conditions at the top and bottom play therein a crucial role.

More recently, the help of direct numerical simulations (DNSs) has led to a further understanding of the fluid flow inside the turbulent structure. Meseguer *et al.* (2009) discovered that the turbulent spiral originates at the inner cylinder, where vortical structures detach from the wall and spread out radially towards the outer cylinder. For smaller aspect ratios $\Gamma \leqslant 15$ (with $\Gamma = L/d$ the height of the cylinder divided by the gap width) where no turbulent spiral is formed, turbulent bursts were attributed to a secondary instability mechanism of the laminar flow (Coughlin & Marcus 1996). We note however that laminar spirals do form at low Γ, as they also play a central role in the bursting mechanism (Hamill 1995).

By means of conditional averaging over the spiral turbulence domain, Dong (2009) revealed that a strong angular gradient of the streamwise velocity prevails in the spiral structure. Subsequently, Dong & Zheng (2011) found that the spiral domain consists of elongated vortical structures and that the linearly unstable region of the laminar flow contains vortices with a streamwise vorticity. Furthermore, Burin & Czarnocki (2012) simulated spiral turbulence with a stationary inner cylinder, such that the entire flow is linearly stable. Finally, Barkley & Tuckerman (2007) and Tuckerman & Barkley (2011) studied, with the use of DNS, turbulent bands in transitional plane Couette (PC) flow.

1.2. *A pattern forming turbulent spiral*

A new and remarkable insight into the dynamics of the turbulent spiral came from Prigent *et al.* (2002). Their experimental observations of stripes in PC flow and spirals in TC flow at very high radius ratio $\eta = r_i/r_o = 0.98$ reveal a turbulence intensity modulation of these flow states that fits in every respect the phenomenology

of the (complex) Ginzburg–Landau (GL) amplitude equations (van Saarloos 1994; Cross & Greenside 2009). Thereby, the spiral fits the dynamical behaviour of a finite-wavelength instability, originating from the 'featureless turbulent' state. The GL equation describes the time evolution of a complex amplitude $A(x, t)$ of a physical field variable $\boldsymbol{u}(x, t)$

$$\tau_0 \partial_t A(x, t) = \epsilon A + \xi_0^2 \partial_x^2 A - g_0 |A|^2 A, \tag{1.2}$$

where τ_0 is the time scale, ξ_0 is the length scale and g_0 sets the magnitude scale of the structure; ϵ is the reduced bifurcation parameter $\epsilon = (Re_{i,c} - Re_i)/Re_{i,c}$, where $Re_{i,c}$ is the critical inner cylinder Reynolds number at which the bifurcation occurs upon reducing Re_i and the pattern emerges. By rescaling (1.2), one finds that the intensity of the pattern $|A|^2 = O(\epsilon^1)$. Note that Prigent *et al.* (2002, 2003) coupled two GL equations to account for the coexistence of spirals with opposing helicity and added a noise term, to account for the turbulent fluctuations in the background velocity field.

In principle, for a bifurcation to travelling waves, the coefficients on the right-hand side of (1.2) are expected to acquire imaginary parts, in other words, to be complex. These imaginary parts model the shift of the frequency of the modes with ϵ, wavenumber and amplitude. We will not probe these effects here. In fact, as we shall see, the patterns are actually stationary in the frame moving with the mean flow, which indicates that it may be most appropriate to think of the patterns as stationary. This is natural to expect considering that the equations are invariant under continuous translation in the azimuthal and axial directions.

Further work on the GL description of laminar Taylor spirals has been carried out by Goharzadeh & Mutabazi (2010), who measured the GL coefficients. Rolland & Manneville (2011) carried out underresolved simulations of oblique bands in Couette flow. Also, the amplitude in their simulations, defined as the modulus of the first Fourier mode of the streamwise velocity, does obey the phenomenology of the GL model.

In this paper, we set out to investigate spiral turbulent TC flow by means of DNS. In contrast to the experiments of Prigent *et al.* (2002), which were carried out in the limit of very small curvature ($\eta = 0.98$), in our DNSs, curvature effects do play a role ($\eta = 0.91$). To quantify this, we refer to the curvature Obukhov length $L_c = u_\tau/\kappa\omega_i$, with u_τ the friction velocity and $\kappa = 0.39$ the von Kármán constant, as defined in Bradshaw (1969). This length differentiates the flow regions in a turbulent flow where the production of turbulent kinetic energy is governed by shear and where it is governed by curvature of the streamlines. For values above approximately $(r - r_i)/L_c \geqslant$ 0.1, the effects of curvature are pronounced. We find that for $\eta = 0.91$, $0.5d/L_c \approx 0.2$. For $\eta = 0.98$, $0.5d/L_c \approx O(10^{-3})$.

Further, we employ periodic boundary conditions in the axial direction, and thereby exclude effects originating from the end plates, which are responsible for the no-slip axial boundary conditions in experiments. We study the fluid mechanics of the turbulent spirals and investigate whether the GL description of the spirals holds in our simulations.

The paper is organized as follows: in § 2 we present the description of TC flow and the details of the numerical solver. In § 3.1 we study the appearance and disappearance of the spiral structure, followed by § 3.2, in which we look at the impact of the turbulent spiral on the global transport of momentum. In § 3.3 we study the velocity of the spiral pattern. Section 3.4 then presents the GL description of the spiral. The paper ends with conclusions (§ 4).

2. Taylor–Couette flow and numerical procedure

The TC set-up consists of two concentric, independently rotating cylinders with radii r_i and r_o. The gap width d is defined as $d = r_o - r_i$, the radius ratio $\eta = r_i/r_o$ and the aspect ratio as $\Gamma = L/d$, where L is the height of the cylinders. In this paper we keep the radius ratio fixed at $\eta = 0.91$. The aspect ratio Γ varies in the range $42 \leqslant \Gamma \leqslant 125$. For every DNS we simulate the full azimuthal circumference of the TC set-up.

The Navier–Stokes equations that govern the shear-driven fluid flow in between the two concentric rotating cylinders are formulated in cylindrical coordinates and dimensionless form, namely

$$\partial_{\hat{t}}\hat{u}_r + \hat{\boldsymbol{u}} \cdot \hat{\boldsymbol{\nabla}}\hat{u}_r - \frac{\hat{u}_\theta^2}{\hat{r}} = -\partial_{\hat{r}}\hat{P} + \frac{1}{Re_i - Re_o\eta}\left(\hat{\nabla}^2\hat{u}_r - \frac{\hat{u}_r}{\hat{r}^2} - \frac{2}{\hat{r}^2}\partial_{\hat{\theta}}\hat{u}_\theta\right), \qquad (2.1)$$

$$\partial_{\hat{t}}\hat{u}_\theta + \hat{\boldsymbol{u}} \cdot \hat{\boldsymbol{\nabla}}\hat{u}_\theta + \frac{\hat{u}_r\hat{u}_\theta}{\hat{r}} = -\frac{1}{\hat{r}}\partial_{\hat{\theta}}\hat{P} + \frac{1}{Re_i - Re_o\eta}\left(\hat{\nabla}^2\hat{u}_\theta - \frac{\hat{u}_\theta}{\hat{r}^2} + \frac{2}{\hat{r}^2}\partial_{\hat{\theta}}\hat{u}_r\right), \qquad (2.2)$$

$$\partial_{\hat{t}}\hat{u}_z + \hat{\boldsymbol{u}} \cdot \hat{\boldsymbol{\nabla}}\hat{u}_z = -\partial_{\hat{z}}\hat{P} + \frac{1}{Re_i - Re_o\eta}(\hat{\nabla}^2\hat{u}_z), \qquad (2.3)$$

$$\hat{\boldsymbol{\nabla}} \cdot \hat{\boldsymbol{u}} = 0. \qquad (2.4)$$

The differential operators are defined as: $(\boldsymbol{u} \cdot \boldsymbol{\nabla})f = (u_r\partial_r + u_\theta(1/r)\partial_\theta + u_z\partial_z)f$ and $\nabla^2 f = (1/r)\partial_r(r\partial_r f) + (1/r^2)\partial_\theta^2 f + \partial_z^2 f$. The boundary conditions are $u_\theta|_{r_i} = r_i\omega_i$ and $u_\theta|_{r_o} = r_o\omega_o$, $(u_z, u_r)|_{r_i} = 0$ and $(u_z, u_r)|_{r_o} = 0$. In the axial direction we employ periodic boundary conditions. Here, $Re_i = r_i\omega_i d/\nu$ and $Re_o = r_o\omega_o d/\nu$ are the inner and outer cylinder Reynolds numbers, respectively, where by definition $\omega_i \geqslant 0$. Note that the equations can also be written in terms of the Taylor number and a geometric Prandtl number, highlighting the analogy with Rayleigh–Bénard convection (Grossmann, Lohse & Sun 2016). The velocity vector $\boldsymbol{u}$ comprises (u_θ, u_z, u_r), respectively the streamwise, spanwise and wall-normal velocity, which in this paper are normalized by the inner cylinder azimuthal velocity $u_{\theta,i}$. Hatted symbols represent dimensionless variables, where velocity, length and time are made dimensionless as, respectively, $u = r_i|\omega_i - \omega_o|\hat{u}$, $r = d\hat{r}$ and $t = (d/(r_i|\omega_i - \omega_o|))\hat{t}$ and pressure is made dimensionless accordingly, $P = \rho r_i^2|\omega_i - \omega_o|^2\hat{P}$.

The equations are spatially discretized to second order and are solved on a finite difference grid (Verzicco & Orlandi 1996). Time integration is performed with a fractional-step third-order Runge–Kutta scheme. For more details of the numerical code we refer the reader to van der Poel *et al.* (2015) and Ostilla-Mónico *et al.* (2013). Grid independence checks are carried out to ensure sufficient numerical resolution. Time convergence is controlled by monitoring the torque on both cylinders, which is expressed in dimensionless form as the Nusselt number Nu_ω,

$$Nu_\omega = \frac{J^\omega}{J^\omega_{lam}} = \frac{\mathcal{T}(2\pi L\rho)^{-1}}{2\nu r_i^2 r_o^2 \frac{\omega_i - \omega_o}{r_o^2 - r_i^2}}, \qquad (2.5)$$

where $J^\omega = r^3(\nu\partial_r\langle\omega\rangle_{A(r),t} + \langle u_r\omega\rangle_{A(r),t})$ is the angular velocity flux, $\langle.\rangle_{A(r),t}$ represents averaging over a cylinder surface $A(r)$ and time t, $J^\omega_{lam} = 2\nu r_i^2 r_o^2((\omega_i - \omega_o)/(r_o^2 - r_i^2))$ is the laminar angular velocity flux and $\mathcal{T}$ is the torque.

Alternatively to Nu_ω, we define the friction factor C_f,

$$C_f = \frac{G}{(Re_i - \eta Re_o)^2} = \frac{2\pi Nu_\omega J^\omega_{lam}}{\nu^2(Re_i - \eta Re_o)^2}, \qquad (2.6)$$

where $G = \mathcal{T}/(\rho \nu^2 L)$ is the dimensionless torque; C_f is thus the ratio of the wall stress over the kinetic energy of the flow.

3. Results and discussion

3.1. *Turbulent spirals: their formation and disappearance*

When the destabilizing effects of inner cylinder rotation become large compared to the stabilizing effects of outer cylinder rotation, TC flow can enter the 'featureless turbulent' regime, see figure 1. Although the flow is turbulent throughout the domain, the term 'featureless turbulence', as mentioned in Andereck *et al.* (1986), is deceiving, since the mean flow does contain structures with streamwise vorticity, i.e. the turbulent Taylor vortex (Huisman *et al.* 2014).

We run a DNS of the 'featureless turbulent' regime, with $Re_i = 800$ and $Re_o = -1200$, of which three snapshots of the streamwise/azimuthal velocity at varying radii are presented in figure 2 (*a–c*). As initial conditions for all our simulations we use the laminar solution of TC flow (Grossmann *et al.* 2016) plus small spatial perturbations to the radial velocity component $u_r = 0.1 r_i \omega_i \sin(2\pi z/L)$, with z the axial coordinate and the axial velocity component $u_z = 0.1 r_i \omega_i \sin((r - r_i)2\pi/d)(1 - |\sin(2\pi z/L)|)\sin(2\pi z/L)$. The resolution is set to $N_\theta \times N_z \times N_r = 768 \times 1280 \times 80$ at $\Gamma = 64$, such that we resolve the global Kolmogorov scale $\eta_k = 0.03d$, where $\eta_k = (\nu^3/\epsilon_\nu)^{1/4}$, with ϵ_ν the mean kinetic dissipation rate. The spacing of the finite size grid at the wall in the radial direction is $0.44 y_0$, where y_0 is the viscous length scale $y_0 = \nu/\sqrt{\tau_w/\rho}$, with ν the kinematic velocity, ρ the fluid density and τ_w the wall shear stress. With varying Γ, we change $N_z = 1280(\Gamma/64)$ while $N_\theta \times N_r = 768 \times 80$ for all simulations.

In figure 2 we observe long, thin, meandering patterns in the azimuthal velocity u_θ. The structures have a length scale $\approx (0.5 - 1.0)d$ in the axial direction and are more distinct close to the inner cylinder at $r = r_i + 0.25d$, whereas they become more diffuse closer to the outer cylinder at $r = r_i + 0.75d$. The nodal plane of neutral stability (defined by the laminar azimuthal velocity being zero $u_{\theta,lam} = 0$), is at $r_n = r_o \sqrt{((Re_i - \eta Re_o)/(Re_i - \eta^{-1}Re_o))} \approx 1.04 r_i$ for $Re_i = 800$ and $Re_o = -1200$, such that the inner region of the domain $r < 1.04 r_i$ is linearly unstable and the outer region of the domain $r > 1.04 r_i$ is linearly stable (Lord Rayleigh 1916). This is confirmed in figure 3(*a*), where we present contours of the instantaneous azimuthal velocity $u_\theta = u_\theta(\theta, z, r, t)$ in a small portion of the axial–radial plane at $Re_i = 800$ and $Re_o = -1200$. We find vortical structures, with a streamwise vorticity and length scale $\approx (0.5 - 1.0)d$ close to the inner cylinder. These structures resemble Taylor vortices, although they do not close the entire circumferential direction of the domain, see figure 2. The region $r > r_n$ does exhibit chaotic fluid flow motion, triggered by the instabilities from the inner region. This is reminiscent of the so-called inner–outer region interaction as described by Coughlin & Marcus (1996). As such, we find that, for $Re_i = 800$, the entire domain is filled with chaotic (turbulent) fluid motion, and hence falls into the 'featureless turbulent' part of the above phase space, see figure 1.

Starting from this state (figure 2*a–c*), we decrease Re_i to $Re_i = 750$ (figure 2*d–f*), while keeping $Re_o = -1200$. We run the simulations until the flow is statistically stationary, i.e. when the dimensionless torque $\langle Nu_\omega \rangle_t$, calculated at both cylinders, is constant to within 1 %, where $\langle . \rangle_t$ indicates time averaging over $50\hat{t}$. Resulting from the decrease in shear, the flow starts to laminarize at the outer cylinder, see figure 3(*b*). However, the flow remains turbulent throughout the majority of the domain, as seen in figure 2(*d–f*). Interestingly, we find in these turbulent parts of the flow, in the contours
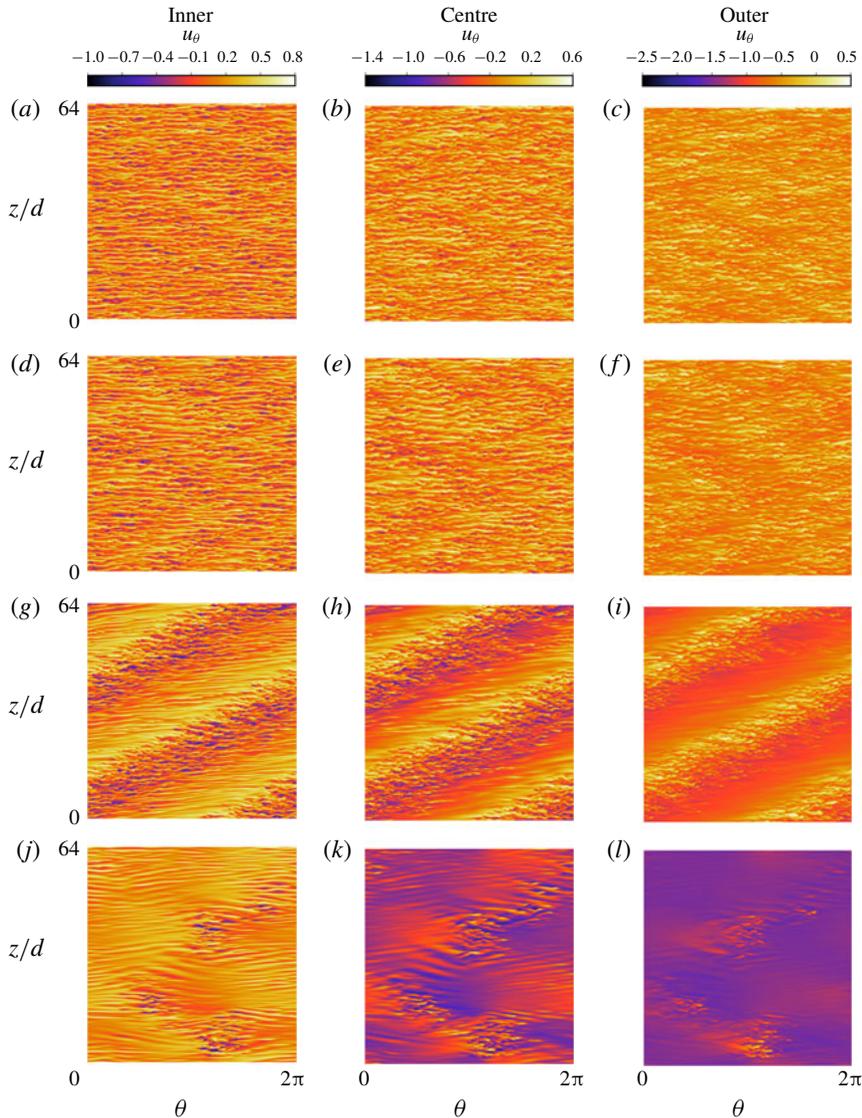
FIGURE 2. Snapshots of the azimuthal velocity u_θ, close to the inner cylinder ($r = r_i + d/4$), at the centre ($r = r_i + d/2$) and close to the outer cylinder ($r = r_i + 3d/4$) for $Re_o = -1200$ and for different $Re_i = 800$ (a–c), 750 (d–f), 700 (g–i) and 524 (j–l). The horizontal axis gives the angle θ. On the vertical axis the axial coordinate z is normalized with the gap width. From a chaotic turbulent base flow (a–c), the finite-wavelength instability forms (panels d–f and in particular g–i). Further away from the transition an isolated stripe (spiral) breaks down in connected and isolated turbulent spots (j–l).

of $u_\theta(\theta, z, r, t)$, the appearance of diagonal coherent patterns. At this Re_i, the patterns exist at opposing angles and 'nucleate' at varying places.

Subsequently, we further lower Re_i to $Re_i = 700$ (figure 2, g–l) for which one well-defined turbulent spiral pattern emerges. At $r = r_i + 0.75d$, the spiral contains turbulent motion, whereas the region in between the turbulent spiral bands is laminarized and
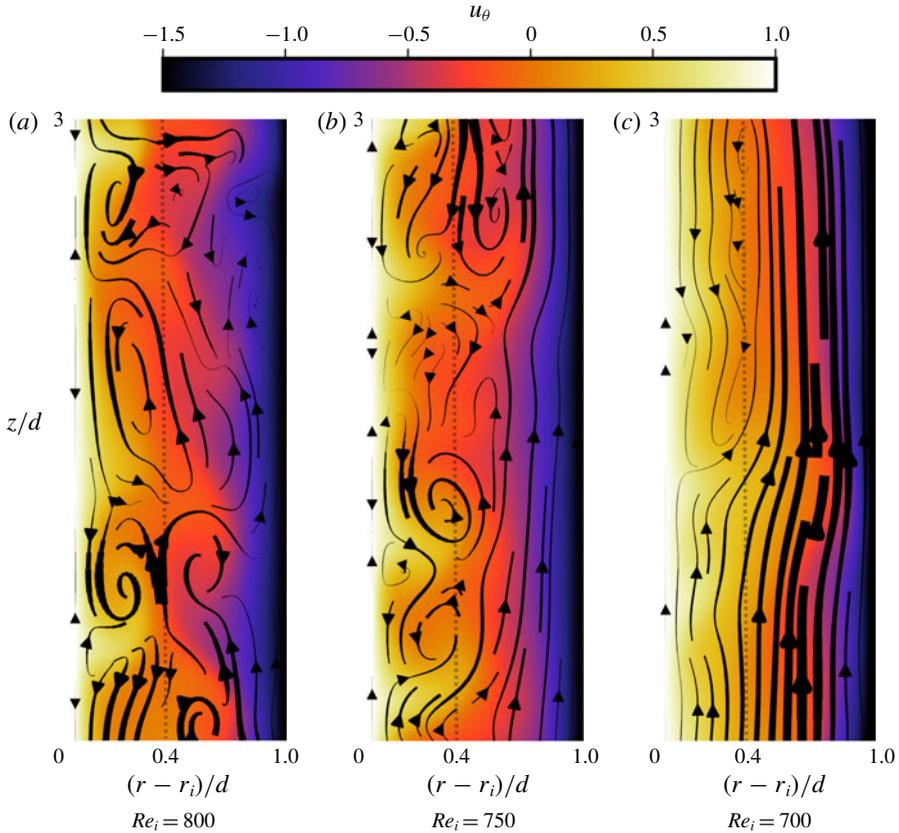
FIGURE 3. Streamlines overlay snapshots of the azimuthal velocity u_θ in the meridional plane for $Re_o = -1200$. The thickness of the streamlines represents the norm of the velocity vector (u_r, u_z). We observe chaotic motion for all r in the 'featureless turbulent' flow (*a*). With decreasing Re_i, laminarization occurs from the outer cylinder towards the inner cylinder (*b*,*c*). The vertical dashed lines at $(r - r_i)/d \approx 0.4$ give the location of the nodal plane of neutral stability. The meridional snapshots where obtained at $\theta = \pi$.

contains no vorticity, see figure 3(*c*). Note that the regions of maximal intensity of the banded structure is shifted to the right somewhat as one moves outwards (this is most clearly visible for $Re_i = 700$). This is in agreement with the results of Meseguer *et al.* (2009) for the structure of turbulent bands. Close to the inner cylinder, the spiral also contains turbulent motions, however, the region in between the turbulent spiral bands does contain Taylor-like vortices. Figure 3(*c*) presents a section of the turbulent spiral corresponding to $0 \leqslant z/d \leqslant 3$ in figure 2 (third row). For an extensive range of $530 \leqslant Re_i \leqslant 700$, the spiral remains present in the flow. Lowering Re_i even further, e.g. to $Re_i = 524$ (see figure 2*j*–*l*), makes the spiral lose coherence. The flow then contains intermittent 'puffs' of chaotic motion in an otherwise laminar base flow. We have carried out several numerical simulations around $Re_i = 524$, namely with $Re_i = $ [490, 500, 510, 520, 522, 524, 526, 528, 530] in order to locate the critical Reynolds number $Re_{i,crit}$ at which the turbulence can be sustained. For simulation times as long as $T \approx 1000(d/r_i(\omega_i - \omega_o))$, we find that the puffs are only sustained at $Re_i \geqslant 524$. The dynamics of the spatio-temporal intermittent, incoherent, 'puffs' is, however, not the
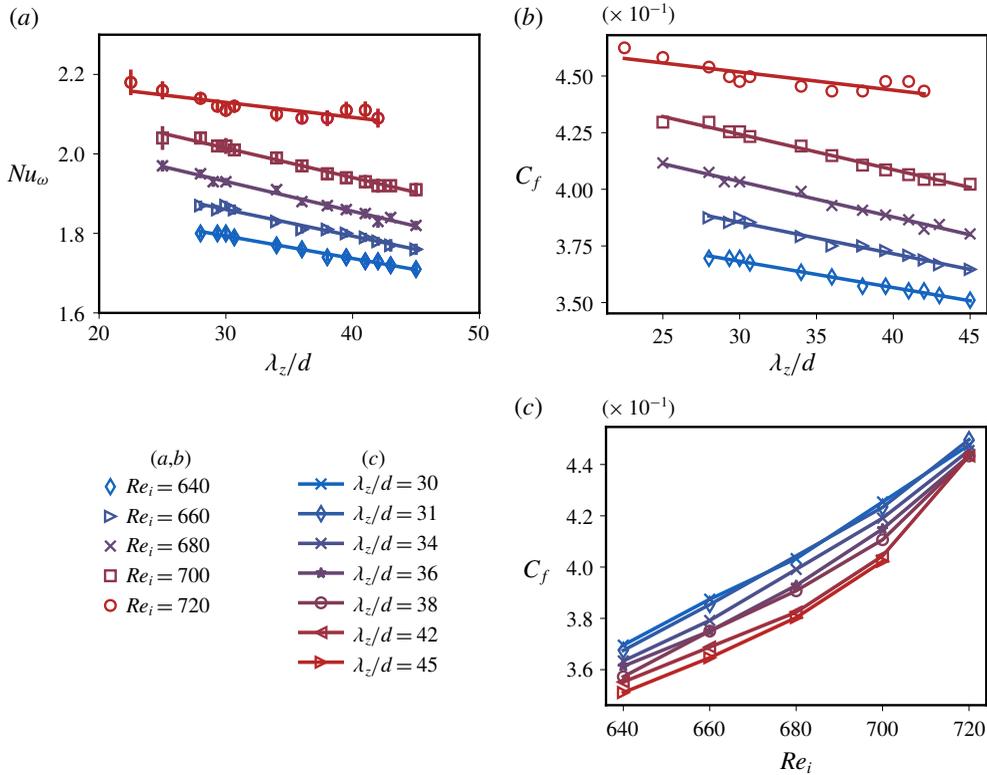
FIGURE 4. (*a*) Dimensionless angular velocity transport Nu_ω versus the wavelength λ_z/d of the turbulent spiral for different Reynolds numbers. Nu_ω decreases linearly with increasing wavelength, which is attributed to the decrease in turbulence fraction in the domain, with increasing axial wavelengths of the spiral. (*b*) The friction factor C_f for different Reynolds numbers versus λ_z/d. (*c*) C_f versus the inner cylinder Reynolds number Re_i for $Re_o = -1200$. An increase of C_f indicates transitional behaviour from the laminar to the turbulent regime.

focus of this study. In the remainder, we will study the dynamics in that part of the phase space where the spiral is still coherent.

3.2. *Dynamics of the turbulent spiral*

The influence of the turbulent spiral structure on the momentum transport is not addressed in the literature. In this section we will study the global response for both varying spiral wavelength λ_z and varying Re_i, while we keep $Re_o = -1200$. To vary λ_z, we simulate 20 cases of varying aspect ratio $42 \leqslant \Gamma = L/d \leqslant 125$ of the TC set-up. In the axial direction we employ periodic boundary conditions, such that $\lambda_z = \Gamma/n$, with n a positive integer that represents the number of windings of the spiral around the inner cylinder. We find a range of $26 \leqslant \lambda_z/d \leqslant 45$, whereby up to three spirals fit into the domain for a given Γ. When we examine the mean velocity and the mean turbulent intensity, we do not find any influence of Γ on the flow for fixed λ_z/d. In other words, the flow at $\Gamma = 84$ with two spirals of $\lambda_z/d = 42$ is statistically identical to the flow at $\Gamma = 42$ with one spiral of the same $\lambda_z/d = 42$.
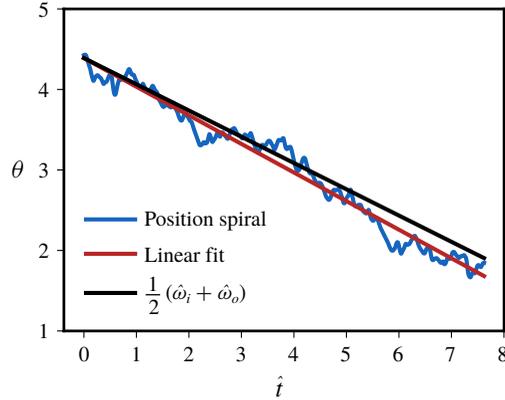
FIGURE 5. Angular location θ of the turbulent spiral versus time $\hat{t}$. The vertical axis represents the angular position of the maximum turbulent intensity at $z = L/2$ and $r = r_i + d/2$. The horizontal axis represents dimensionless time $\hat{t} = t/T$. $\langle\hat{\omega}\rangle_{r,\theta,z}$ is the calculated mean angular velocity in the domain. Excellent agreement between $\Delta\theta/\Delta\hat{t} = -0.355$ and $\langle\hat{\omega}\rangle_{r,\theta,z} = -0.354$ reveals that the spiral is stationary in the reference frame of the mean angular velocity $\langle\hat{\omega}\rangle_{\theta,z,r,t}$. Note that $\frac{1}{2}(\hat{\omega}_i + \hat{\omega}_o) = -0.326$, solid black line, does not match $\Delta\theta/\Delta\hat{t}$.

There is, however, a strong dependence of the global angular momentum transport – expressed in dimensionless form in (2.5) – on the axial wavelength of the spiral. Figure 4(a) presents Nu_ω versus λ_z/d for varying Re_i. With increasing λ_z/d, the turbulence fraction in the domain decreases, resulting in a predominantly diffusive, less efficient, transport of momentum. Figure 4(b) presents the corresponding C_f versus λ_z/d, see (2.6).

The graphical representation of $C_f(Re_i)$ is commonly referred to as the 'Moody' diagram (Moody 1944). Whereas the laminar part of the diagram can be derived analytically, the turbulent part is empirically fitted with the celebrated Prandtl's friction law. For inner cylinder rotation, linearly unstable, TC flow, $C_f(Re_i)$ is monotonically decreasing in the transition region between the laminar and turbulent flow (Lathrop, Fineberg & Swinney 1992). For counter-rotating TC flow, where the transition to turbulence is subcritical and 'catastrophic', we find that $C_f(Re_i)$ is increasing in the transitional region, see figure 4(c). This is reminiscent of the transition scenario in pipe flow, where the sudden appearance of spatio-temporally intermittent turbulence leads to an increase in $C_f(Re)$ (Pope 2000).

3.3. Angular velocity of the spiral

Surprisingly, the angular velocity of the spiral ω_s has hitherto received only little attention in literature. Van Atta (1966) was the first to investigate ω_s and found that it scales with the mean angular velocity of the two cylinders $\omega_s \approx \frac{1}{2}(\omega_i + \omega_o)$ for $Re_i = O(10^3)$, $Re_o < -10^4$. Later, Andereck *et al.* (1986) investigated ω_s for much lower $Re_i = O(10^3)$, $Re_o = -3500$, and found $\omega_s \approx \omega_o$. For laminar interpenetrating spirals Goharzadeh & Mutabazi (2010) found that $\omega_s = \omega_o$. However, the analysis of Prigent & Dauchot (2000) (for similar values of Re_i, Re_o as in this work) showed that $\omega_s = 0.98\omega_m - 0.02\omega_i$, where $\omega_m = \frac{1}{2}(\omega_i + \omega_o)$. In our present DNSs we have access to the full velocity field, in contrast to the experimental work. Thereby we monitor the
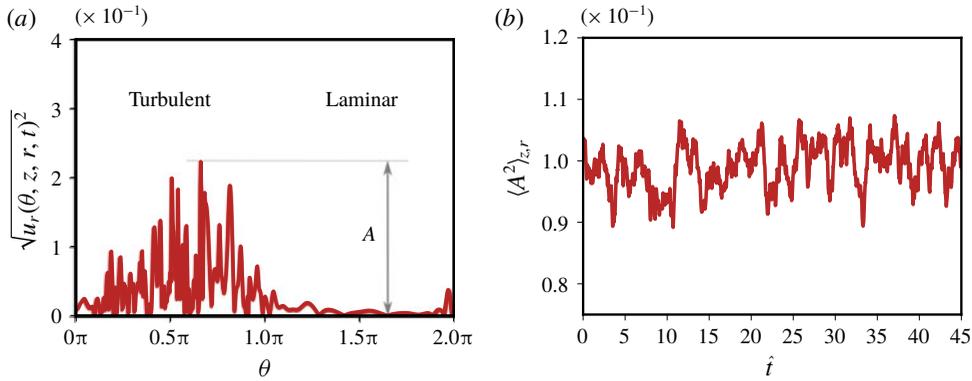
FIGURE 6. Definition of the amplitude A. (*a*) Plot of the square root of the radial velocity component squared $\sqrt{u_r(\theta, z, r, t)^2}$ versus the angular position at $r = r_i + d/2$ and $z = L/2$ at an arbitrary instant in time when the flow is statistically stationary. The amplitude is defined as $A(z, r, t) = (\sqrt{u_r(z, r, t)^2})_{max} - (\sqrt{u_r(z, r, t)^2})_{min}$. (*b*) The time dependent signal. To obtain the converged amplitude, we employ time averaging and we average over spatial coordinates $(r_i + d/4) < r < (r_i + 3d/4)$ and for all z. This particular signal is acquired for $Re_i = 660$ and $Re_o = -1200$.

position of the maximum turbulence intensity in the spiral and from the translation of that position in time extract ω_s, see figure 5. We find that ω_s is not equal to the mean rotation rate, $\frac{1}{2}(\omega_i + \omega_o)$, but instead equals the mean angular velocity in the domain $\langle\omega\rangle = \langle\omega\rangle_{\theta, z, r, t}$. Note that the difference between $\langle\omega\rangle$ and ω_s is only minor and could easily be missed in experiments. In fact, we think that the consistent mismatch between ω_m and ω_s, as found in figure 5 in Prigent & Dauchot (2000), is explained by the mismatch between ω_m and $\langle\omega\rangle$.

3.4. *Amplitude modulation*

3.4.1. *The amplitude*

To describe the turbulent spiral as a pattern forming instability above a critical bifurcation point $\epsilon = 0$, we introduce a perturbation $A(z, t)e^{(ikz - i\omega t)}$ to the base flow u_b. Here, we treat the instability in the axial coordinate direction only. Note that the instability contains both parity symmetry (flipping of the streamwise or axial coordinate directions) and translational symmetry. We define the perturbed physical field u as the root mean square (r.m.s.) of the radial velocity component (in contrast to Prigent *et al.* (2002), who define u as the r.m.s. of the axial velocity).

Figure 6(*a*) exhibits the instantaneous $u_{r,rms}$ over a line encircling the inner cylinder at $r = r_i + 0.5d$ and $z = L/d$. We define the amplitude from the radial component of velocity u_r as $A = (\sqrt{u_r^2})^{max} - (\sqrt{u_r^2})^{min}$ which is a function of $(r, z; t)$. We calculate A at runtime and average over half the gap width $(r_i + d/4) < r < (r_i + 3d/4)$ and the full height z. Figure 6(*b*) presents the time signal of the spatially averaged squared amplitude $\langle A^2\rangle_{z,r}$. Significant fluctuations of $\langle A^2\rangle_{z,r}$ force us to also take long averages of $\hat{\tau}_{av} \approx 50$. The width of the turbulent spiral Δ_s is approximately $(r_i + 0.5d)\pi$.

We measure the amplitude versus the bifurcation parameter ϵ at a fixed aspect ratio $\Gamma = 64$, and hence a fixed $\lambda_z/d = 32$. For a stationary, finite-wavelength instability, for which the modulation of the amplitude is described by (1.2), we expect $A^2 \propto \epsilon^1$ (Cross & Greenside 2009). Indeed, this scaling is found by Prigent *et al.* (2002), who
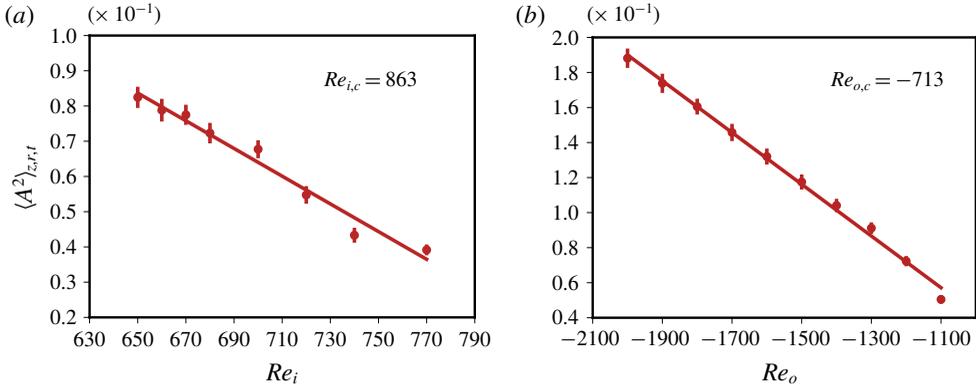
FIGURE 7. Amplitude scaling of the turbulent spiral with varying ϵ. (*a*) Scaling of the amplitude squared A^2 with varying $Re_i(Re_o = -1200)$. The fit highlights that $A^2 \propto \epsilon^1$, with $\epsilon = (Re_{i,c} - Re_i)/Re_{i,c}$, as predicted by the GL equations. Extrapolation of the fit gives $Re_{i,c} = 863$, which compares very well with the experimental results in Prigent *et al.* (2002) for $\eta = 0.98$. (*b*) Scaling of A^2 with varying $Re_o(Re_i = 680)$. We observe an identical scaling for A^2; $A^2 \propto \epsilon^1$, now with $\epsilon = (Re_{o,c} - Re_o)/Re_{o,c}$ and $Re_{o,c} = -713$. Error bars represent the standard deviation of $\langle A^2 \rangle_{z,r}(t)$.

(for different $\eta = 0.98$) extracted a critical $Re_{i,c} = 857 \pm 5$ at which the instability occurs. Figure 7(*a*) shows that we also observe $A^2 \propto \epsilon^1$ over a range of ϵ, close to the bifurcation point. With $Re_o = -1200$ we obtain $Re_{i,c} = 863$, in very close agreement with Prigent *et al.* (2002), in spite of different η. For $Re_i > 780$, nucleation of domains of opposing helicity, and the appearance of turbulence in the laminar spiral regions, obscures the precise measurements of the amplitude of the turbulence intensity signal. Prigent *et al.* (2002) were still able to extract the amplitude for these Re due to the very long runtime in the experiments, which at these Γ are not accessible for DNSs. As for $Re_i = 770$, the amplitude is still 0.04, we conclude that the noise term is certainly high.

In a similar manner, we also approach the boundary of the spiral turbulent regime in figure 1 from the horizontal direction, i.e. by varying Re_o and maintaining $Re_i = 680$. For decreasing Re_o, the stabilizing stratification of centrifugal pressure increases, the flow laminarizes and the spiral emerges. As such, we define $\epsilon = (Re_{o,c} - Re_o)/Re_o$. Figure 7(*b*) convincingly indicates that, also for varying Re_o, $A^2 \propto \epsilon^1$, with $Re_{o,c} = -713$. This indicates that the turbulent spiral behaves as a finite-wavelength instability, in spite of the curvature effects.

3.4.2. *The instability diagram*

By carefully varying the aspect ratio Γ we are able to study a variation in the axial wavelength λ_z of the spiral in the domain $26 \leqslant \lambda_z/d \leqslant 45$. Considering that we do probe the amplitude of a stationary turbulent spiral versus the wavelength, and the influence of the wavelength of the momentum transport, we do not imply that for a certain aspect ratio only one such wavelength exists. In fact, it is most likely that the wavelength of the spiral is sensitive to initial conditions, as also the wavelength of the Taylor–Vortex is. With axially periodic boundary conditions, we do not find any Reynolds number dependence of λ_z, neither on Re_i nor on Re_o, since $\lambda_z = \Gamma/n$. In contrast, such a dependence was experimentally observed by Prigent & Dauchot
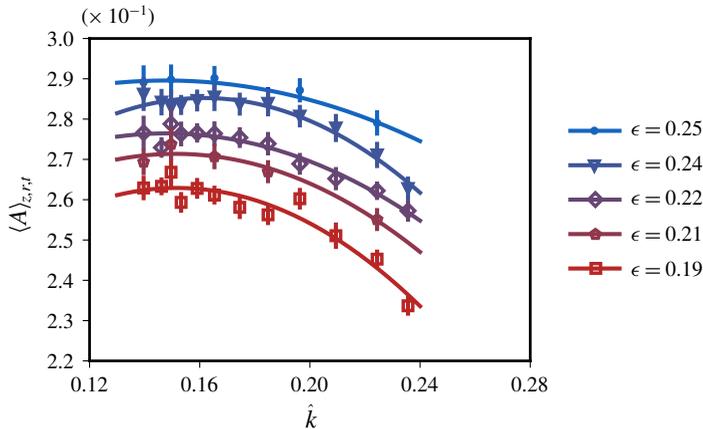
FIGURE 8. Amplitude A of the finite-wavelength instability versus wavenumber $\hat{k}$ for varying reduced thresholds $\epsilon = (Re_{i,c} - Re_i)/Re_{i,c}$. We include all simulations, with varying aspect ratios of $42 \leqslant \Gamma \leqslant 125$. Note that for large aspect ratios multiple spirals exist. Therefore, we cannot simulate smaller wavenumbers than indicated in the graph. We observe consistent behaviour of the amplitude with increasing ϵ, following the phenomenology of a finite-wavelength instability. We fit a second-order polynomial through the data. From this fit we obtain the most unstable wavelength for each ϵ – thus five values in total. We obtain $38.91d < \lambda_c < 42.52d$ with $\text{mean}(\lambda_c) = 41.38d$ and $\text{var}(\lambda_c) = 1.74d$. As we do not observe a systematic trend in the difference between the data and the fit, but rather find that the error is of similar order for all wavenumbers $\hat{k}$, we conclude that a parabolic fit is justified.

(2000) for no-slip boundary conditions at the plates and a much larger system $\Gamma = 430$. Figure 8 presents the amplitude versus the wavenumber $k = 2\pi/\lambda_z$ for increasing ϵ. Note that Re_i and Re_o are identical to those in figure 4, except for $Re_i = 720$, which is excluded here due to the very high noise originating from the 'featureless' turbulent flow.

The parabolic shape, with a maximum around $\lambda_{z,c}/d = 41 \pm 2$, represents the characteristic band of unstable wavenumbers for a finite-wavelength instability above onset. Thereby, we do observe the dependence of A on the bifurcation parameter ϵ, such that an increasing band of wavenumbers becomes unstable with increasing ϵ. We conclude that the most unstable wavelength $\lambda_{z,c}/d \approx 41$ for our simulations at $\eta = 0.91$ differs from the most unstable wavelength $\lambda_{z,c}/d \approx 32$ found in Prigent *et al.* (2002) at $\eta = 0.98$.

In knowing that the amplitude in figure 8 is described by $A^2 = (\epsilon - \xi_0^2(k - k_c)^2)/g_0$, we can also extract the interaction strength coefficient $g_0 = \epsilon/\max_k(A^2)$ and the coherence length coefficient ξ_0 from the fits for varying ϵ. We find that $g_0 = 2.80 \pm 0.11$ and does not depend on ϵ, i.e. it does not depend on the magnitude of the noise, as also found in Prigent *et al.* (2003). The curvature we find at k_c (i.e. $\xi_0^2/g_0 \approx 1.5$) is comparable to the values observed by Prigent *et al.* (2002) (i.e. $\xi_0^2/g_0 \approx 0.5$), but unfortunately our data are not precise enough to extract the coherence length ξ_0 of the pattern with sufficient accuracy to study the trends with ϵ. It is interesting to note that, in doing so, we are in principle able to extract properties of the full amplitude and pattern (like ξ_0) within the GL framework from an analysis of a single mode with fixed wavenumber (the Landau–Hopf or

Stuart–Landau framework) induced by varying the aspect ratio, and that the resulting coherence length is much larger than our system size.

4. Summary and conclusions

In conclusion, we performed direct numerical simulations of counter-rotating Taylor–Couette flow at $400 \leqslant Re_i \leqslant 1200$ and $-2000 \leqslant Re_o \leqslant -1000$. For the aspect ratio Γ of the domain $42 \leqslant \Gamma = L/d \leqslant 125$ with periodic boundary conditions in the axial direction, and the radius ratio $\eta = r_i/r_o = 0.91$. In this regime we found the coexistence of spatio-temporal intermittent laminar and turbulent domains, commonly referred to as spiral turbulence (Coles 1965; Van Atta 1966).

The formation of the turbulent structure (i.e. spiral in TC) out of a turbulent base flow is similar to the phenomenology of the (complex) Ginzburg–Landau equations with a noise term (Prigent *et al.* 2002), in the limit of very low curvature ($\eta = 0.98$). With these fully resolved simulations, we showed that the GL phenomenology also holds for the spirals when curvature effects do play a role. We found that the GL description for pattern formation holds close to the bifurcation point for both varying Re_i and varying Re_o. This, once more, suggests the existence of a finite-wavelength instability in a fully turbulent flow.

Also, we found that the pattern is stationary in the reference frame of the mean angular velocity in the domain $\omega_s = \langle \omega \rangle$. This is in contrast to findings by Prigent & Dauchot (2000) and Andereck *et al.* (1986), who experimentally found that the spiral moves with the mean velocity of the two rotating cylinders, i.e. $\omega_s = \frac{1}{2}(\omega_i + \omega_o)$. However, note that the small difference between $\langle \omega \rangle$ and $\frac{1}{2}(\omega_i + \omega_o)$ is hard to observe in experiments at these low Reynolds numbers.

In contrast with Prigent *et al.* (2002) we have periodic boundary conditions in the axial direction. As such, we only allow a wavelength which is an integer division of the aspect ratio Γ. It is therefore very likely that we do not observe a Reynolds number dependence of λ_z. In their experiment, Prigent *et al.* (2002), however, employ no-slip boundary conditions on the vertical axis, and as such, allow for any wavelength to exist. Despite the different boundary conditions we find strong agreement in the critical Reynolds number at which the instability occurs (i.e. $Re_{i,c} = 863$ for our DNS and $Re_{i,c} = 857$ for the experiments in Prigent *et al.* (2002)) as we also find similar values of the interaction strength $\xi_0^2 \approx 1$ for both. Whereas we obtain k_c by altering the aspect ratio, and Prigent *et al.* (2002) from analysis of monodomain regions in the flow, we both find a parabolic trend of the amplitude with k, where k_c does not appear to depend on Re.

The most unstable wavelength of the instability is found to be $\lambda_{z,c} \approx 41d$, thereby differing from findings in plane Couette flow and in TC flow, where it is $\lambda_{z,c} \approx 32d$ at very high $\eta = 0.98$. Apparently, $\lambda_{z,c}$ is a function of the radius ratio η. This finding may be an important clue for further theoretical investigations, and it may point the way towards understanding the modulated turbulent states in terms of a stationary bifurcation.

Whereas a formal derivation of the instability from the turbulent base flow seems hopeless, since it requires a closed description of the turbulence, fully resolved simulations help to uncover the characteristics and ingredients of the instability when it appears or disappears in the flow. Future work could continue on this road, by e.g. studying the response of the structure to abrupt changes in the boundary conditions, or by studying the effects of initial conditions on the turbulent spiral.

Declaration of interests

The authors report no conflict of interest.

REFERENCES

ANDERECK, C. D., LIU, S. S. & SWINNEY, H. L. 1986 Flow regimes in a circular Couette system with independently rotating cylinders. *J. Fluid Mech.* **164**, 155–183.

BARKLEY, D. 2016 Theoretical perspective on the route to turbulence in a pipe. *J. Fluid Mech.* **643**, 495–507.

BARKLEY, D. & TUCKERMAN, L. S. 2005 Computational study of turbulent laminar patterns in Couette flow. *Phys. Rev. Lett.* **94** (1), 014502.

BARKLEY, D. & TUCKERMAN, L. S. 2007 Mean flow of turbulent-laminar patterns in plane Couette flow. *J. Fluid Mech.* **576**, 109–137.

BRADSHAW, P. 1969 The analogy between streamline curvature and buoyancy in turbulent shear flow. *J. Fluid Mech.* **36**, 177–191.

BURIN, M. J. & CZARNOCKI, C. J. 2012 Subcritical transition and spiral turbulence in circular Couette flow. *J. Fluid Mech.* **709**, 106–122.

COLES, D. 1965 Transition in circular Couette flow. *J. Fluid Mech.* **21**, 385.

COUGHLIN, K. & MARCUS, P. S. 1996 Turbulent bursts in Couette–Taylor flow. *Phys. Rev. Lett.* **77** (11), 2214–2217.

CROSS, M. & GREENSIDE, H. 2009 *Pattern Formation and Dynamics in Nonequilibrium Systems*. Cambridge University Press.

DONG, S. 2009 Evidence for internal structures of spiral turbulence. *Phys. Rev.* E **80**, 067301.

DONG, S. & ZHENG, X. 2011 Direct numerical simulation of spiral turbulence. *J. Fluid Mech.* **668**, 150–173.

ESSER, A. & GROSSMANN, S. 1996 Analytic expression for Taylor–Couette stability boundary. *Phys. Fluids* **8**, 1814–1819.

FEYNMAN, R. P. 1964 *Lecture Notes in Physics*, vol. 2. Addison-Wesley.

GOHARZADEH, A. & MUTABAZI, I. 2010 Measurement of coefficients of the Ginzburg–Landau equation for patterns of Taylor spirals. *Phys. Rev.* E **82**, 016306.

GROSSMANN, S., LOHSE, D. & SUN, C. 2016 High Reynolds number Taylor–Couette turbulence. *Annu. Rev. Fluid Mech.* **48**, 53–80.

HAMILL, C. F. 1995 Turbulent bursting in the Couette–Taylor system. MA thesis, University of Texas at Austin.

HEGSETH, J. J., ANDERECK, C. D., HAYOT, F. & POMEAU, Y. 1989 Spiral turbulence and phase dynamics. *Phys. Rev. Lett.* **62**, 257–260.

HUISMAN, S. G., VAN DER VEEN, R. C. A., SUN, C. & LOHSE, D. 2014 Multiple states in highly turbulent Taylor–Couette flow. *Nat. Commun.* **5**, 3820.

LATHROP, D. P., FINEBERG, J. & SWINNEY, H. S. 1992 Transition to shear-driven turbulence in Couette–Taylor flow. *Phys. Rev.* A **46**, 6390–6405.

LORD RAYLEIGH 1916 On the dynamics of revolving fluids. *Proc. R. Soc. Lond.* A **93**, 148–154.

MESEGUER, A., MELLIBOVSKY, F., AVILA, M. & MARQUES, F. 2009 Instability mechanisms and transition scenarios of spiral turbulence in Taylor–Couette flow. *Phys. Rev.* E **80**, 046315.

MOODY, L. F. 1944 Friction factors for pipe flow. *Trans. ASME* **66**, 671–684.

OSTILLA-MÓNICO, R., STEVENS, R. J. A. M., GROSSMAN, S., VERZICCO, R. & LOHSE, D. 2013 Optimal Taylor–Couette flow: direct numerical simulations. *J. Fluid Mech.* **719**, 14–46.

VAN DER POEL, E. P., OSTILLA-MÓNICO, R., DONNERS, J. & VERZICCO, R. 2015 A pencil distributed finite difference code for strongly turbulent wall-bounded flows. *Comput. Fluids* **116**, 10–16.

POPE, S. B. 2000 *Turbulent Flow*. Cambridge University Press.

PRIGENT, A. & DAUCHOT, O. 2000 Barber pole turbulence in large aspect ratio Taylor–Couette flow. arXiv:cond-mat/0009241.

PRIGENT, A., GRÉGOIRE, G., CHATÉ, H. & DAUCHOT, O. 2003 Long-wavelength modulation of turbulent shear flows. *Physica* D **174** (1), 100–113.

PRIGENT, A., GRÉGOIRE, G., CHATÉ, H., DAUCHOT, O. & VAN SAARLOOS, W. 2002 Large-scale finite-wavelength modulation within turbulent shear flows. *Phys. Rev. Lett.* **89** (1), 014501.

ROLLAND, J. & MANNEVILLE, P. 2011 Ginzburg–Landau description of laminar-turbulent oblique band formation in transitional plane Couette flow. *Eur. Phys. J.* B **80**, 529–544.

VAN SAARLOOS, W. 1994 The complex Ginzburg–Landau equation for beginners. In *Proceedings of the Santa Fe Workshop on Spatio-Temporal Patterns in Nonequilibrium Complex Systems* (ed. P. E. Cladis & P. Palffy-Muhoray). Addison-Wesley.

TAYLOR, G. I. 1923 Stability of a viscous liquid contained between two rotating cylinders. *Phil. Trans. R. Soc. Lond.* A **223**, 289–343.

TUCKERMAN, L. S. & BARKLEY, D. 2011 Patterns and dynamics in transitionial plane Couette flow. *Phys. Fluids* **23**, 041301.

VAN ATTA, C. 1966 Exploratory measurements in spiral turbulence. *J. Fluid Mech.* **25** (3), 495–512.

VERZICCO, R. & ORLANDI, P. 1996 A finite-difference scheme for three-dimensional incompressible flow in cylindrical coordinates. *J. Comput. Phys.* **123**, 402–413.